

Manipulation of valley and spin properties in two-dimensional Janus WSiGeZ₄ (Z=N, P, As) through symmetry control

Sajjan Sheoran, Ankita Phutela, Ruman Moullik, and Saswata Bhattacharya
Department of Physics, Indian Institute of Technology Delhi, New Delhi 110016, India

A class of septuple-atomic-layer two-dimensional (2D) materials, MA₂Z₄, is sought as an alternative to 2D hexagonal transition metal dichalcogenides in the field of valleytronics and spintronics. In these materials, the structural symmetry can be varied by changing the stacking of its three parts in the monolayer. We show that in Janus monolayer WSiGeZ₄ (Z=N, P, As), the Berry curvature and Rashba effect are enhanced by modifying the stacking orders. Intrinsic electric field and composition of the *d* orbitals play a dominant role in determining these properties. The vertical field lifts the spin degeneracy along in-plane direction, inducing the Rashba effect around Γ point. The in-plane orbitals under the influence of in-plane electric field contribute to the Zeeman splitting of bands at K/K' points. Berry curvature is strengthened by up to 300% compared to its ground state through symmetry control, along with a significant increment in the Rashba coefficient. Moreover, monolayer WSiGeP₄ and WSiGeAs₄ have multiple valleys, implying another valley-dimension. We construct a symmetry adapted *k.p* Hamiltonian for the valleys and investigate the effect of strain and electric field on the band structure. The interesting spin-valley physics in monolayer WSiGeZ₄ suggests their exceptional potential for spintronics and valleytronics applications.

I. INTRODUCTION

The successful investigation of graphene has spurred the discovery of extraordinary properties and promising applications in the field of two-dimensional (2D) materials [1–3]. Afterwards, numerous 2D materials such as silicene, germanene, boron nitride, transition metal dichalcogenides (TMD) and so on have been explored [4–9]. 2D materials with Janus structure possess different physical and chemical properties on each side due to mirror symmetry breaking, which make them exciting [10, 11]. The asymmetric crystal potential causes an intrinsic electric field in these Janus 2D materials, leading to spin-valley splitting and Rashba spin splitting when combined with spin-orbit coupling (SOC) [12, 13]. Additionally, Janus materials show great applications in photocatalytic water splitting, magnetic skyrmions, and out-of-plane piezoelectricity [14–16]. The experimental synthesis of MoSSe from MoSe₂ through the replacement of Se atom by S atom, further triggered the prediction of more Janus 2D materials [17, 18]. Only TMD and metal monochalcogenides Janus materials have been extensively studied so far. Therefore, it is necessary to expand this family and probe into their physical properties to have a more in-depth understanding.

Recently, the MA₂Z₄ (M=Cr, Mo, W, V, Nb, Ta, Ti, Zr or Hf; A=Si or Ge; and Z=N, P, As) 2D family of the septuple-atomic layer has been proposed [19]. Particularly, 2D van der Waals (vdW) layered MoSi₂N₄ and WSi₂N₄ have been successfully fabricated by the chemical vapor deposition method [20]. It has been found that WA₂Z₄ materials have high tensile strength with excellent ambient stability. Subsequently, several predictions of these Janus 2D materials and their excellent physical properties have been carried out. This includes the quantum spin Hall state in SrAlGaTe₄ [21], high electron mobility, efficient photocatalysis, Rashba spin splitting, out-

of-plane piezoelectricity in the MoSiGeN₄ [22–24] and intrinsic ferromagnetism in the VSiGeN₄ [25, 26]. Therefore, this class of materials is expected to provide intriguing physical phenomena, particularly in valleytronics and spintronics.

Nowadays, spin and valley are considered as extra degrees of freedom, which are distinct from the electronic charge and provide an interesting avenue in semiconductor devices [27, 28]. This draws a great deal of attention to the number of emergent quantum phenomena such as valley Hall effect and valley-dependent orbital magnetic moment. The broken inversion symmetry is compulsory for valleytronics, since Berry curvature vanishes in centrosymmetric materials [29]. Also, strong SOC in inversion asymmetric materials induces Rashba spin splitting, which is a critical ingredient in spin field-effect transistors (SFETs) [30–32]. The charge carriers with Rashba SOC experience a momentum-dependent effective magnetic field, hence a spin-dependent velocity correction term arises [31]. Thus, the Rashba effect is extensively studied for SFETs and spin-to-charge interconversion. The spin-valley locking and the Rashba effect arising from the SOC are bringing tremendous attention to the flourishing field of valleytronics and spintronics. These effects have been noticed in graphene [33], TMDs [27], *h*-MN (M=Nb, Ta) [34] and bismuth thin films [35]. However, the scarcity of 2D materials showing these phenomena with appreciable spin-valley polarization and significant Rashba effect holds back the field of spin valleytronics.

In this article, we have investigated the effect of stacking of A-Z layers to modulate the electronic properties, focusing on their spintronics and valleytronics aspects. We have taken the unexplored Janus WSiGeZ₄ as an example to study these effects. The first-principles calculations predict that these materials have Dirac-type valleys located at the corners of Brillouin zone (BZ), connected

by time-reversal symmetry. The valleys show contrasting physics, i.e., spin polarization, optical circular dichroism and Berry curvature. The broken surface inversion symmetry induces Rashba spin splitting at the center of the BZ. The findings imply that symmetry control enhances Berry curvature by more than 300%. Furthermore, Rashba splitting increases significantly by modifying the out-of-plane asymmetry. The underlying mechanism behind the unconventional enhancement is duly investigated through microscopic orbital contribution and macroscopic charge transfer. This method is more effective compared to the strain and electric field, in modulating the Berry curvature and Rashba splitting. The high carrier mobilities and tunable electronic properties suggest their great potential in spintronics and valleytronics.

II. COMPUTATIONAL METHODS

Density functional theory (DFT) calculations have been carried out to study the electronic properties as implemented in Vienna *ab initio* simulation package (VASP) [36]. Projector augmented waves (PAW) with cutoff energy of 550 eV are employed as a basis set [37, 38]. The Perdew-Burke-Ernzerhof (PBE) parametrization at the level of generalized gradient approximation is used as the exchange-correlation functional [39]. The structures are initially relaxed until the force on each atom is smaller than 1 meV/Å. A vacuum spacing of 18 Å vertical to the layers is maintained to avoid spurious interactions between periodic images. The energy convergence threshold is set to 10^{-6} eV. BZ sampling is done using k -point mesh with a separation of 0.02 \AA^{-1} . Phonon spectra are calculated using the density functional perturbation theory as implemented in VASP alongside PHONOPY [40]. Berry curvatures and spin textures are obtained from the maximally localized Wannier functions as implemented in the Wannier90 [41]. Band gaps are also calculated using the hybrid Heyd-Scuseria Ernzerhof (HSE06) [42] functional and G_0W_0 @PBE method [43, 44]. To appraise the optical spectra, many-body perturbation theory calculations within the framework of G_0W_0 and BSE [45] are performed.

III. RESULTS AND DISCUSSION

A. Crystal structure and electronic properties

WA_2Z_4 structure, built by septuple atomic layers in the sequence Z-A-Z-W-Z-A-Z having D_{3h} point group symmetry, can be regarded as one layer of WZ_2 sandwiched by two layers of A-Z [19]. The intermediate WZ_2 is structurally similar to 1H-TMD [19, 46, 47]. The WA_2Z_4 structure breaks inversion symmetry and preserves horizontal mirror symmetry (σ_h). When they form the Janus structure by replacing A atom with a different

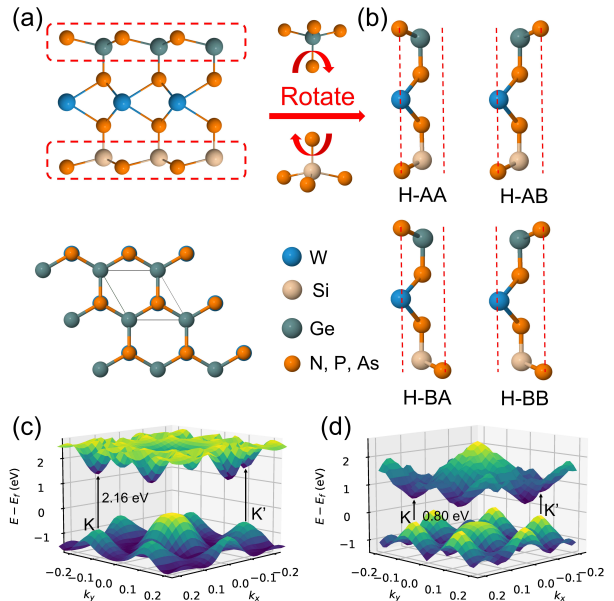


FIG. 1. (a) Side and top views of lattice structure corresponding to monolayer H-BB WSiGeZ₄. (b) Side views of various stacking orders for three constituent parts in the monolayer WSiGeZ₄. The 3D view of the top valence band and bottom conduction band in monolayer (c) H-BB WSiGeN₄ and (d) H-AA WSiGeP₄.

same group atom, σ_h is broken, leading to inversion symmetry breaking with C_{3v} symmetric point group [22, 23]. Figure 1(a) shows the fully optimized crystal structure of the WSiGeZ₄. Theoretically, several intermediate structures are obtained by varying the stacking of the intermediate layer of 1H-WZ₂ and two A-Z layers [19, 20, 48–52]. As shown in Fig. 1(b), we have considered the four structures (H-AA, H-AB, H-BA, and H-BB) depending upon the stacking order of the three constituent (Z-Si, Z-W-Z, and Ge-Z) monolayers. As shown in Table I, the lattice parameters of H-AA, H-AB, H-BA and H-BB are only slightly different. This is because of same coordination environment and similar valence electron states. The lattice constant of Janus WSiGeZ₄ monolayer is approximately the average of WSi₂Z₄ and WGe₂Z₄. It is evident that the lattice constant increases with the increasing atomic number of the pnictogen.

We have obtained the formation energy per atom (E_{for}) to confirm the energy feasibility, using the expression

$$E_{for} = \frac{E_{tot} - (n_W E_W + n_{Si} E_{Si} + n_{Ge} E_{Ge} + n_Z E_Z)}{(n_W + n_{Si} + n_{Ge} + n_Z)} \quad (1)$$

where E_{tot} is the total ground state energy of the WSiGeZ₄ monolayer, E_W , E_{Si} , E_{Ge} , and E_Z are the chemical potentials of W, Si, Ge, and Z atoms, respectively. n_W , n_{Si} , n_{Ge} , and n_Z are the number of W, Si, Ge, and Z atoms in the unit cell, respectively. As clear

TABLE I. Optimized lattice constant (a) for the unit cell of WSiGeZ_4 monolayer. The calculated formation energy per atom (E_{for}), dipole moment per unit cell (P_y , P_z), band gaps in presence of SOC using PBE (E_g^{PBE}) and HSE06 (E_g^{HSE}). The calculated band gaps using G_0W_0 performed on top of PBE functional with inclusion of SOC ($E_g^{\text{GW@PBE}}$).

	Phase	a (Å)	E_{for} (eV)	P_y (eÅ)	P_z (eÅ)	E_g^{PBE} (eV)	E_g^{HSE} (eV)	$E_g^{\text{GW@PBE}}$ (eV)
WSiGeN_4	H-AA	2.929	-0.639	1.710	0.024	2.01	2.48	3.27
	H-AB	2.931	-0.643	-0.930	0.021	1.88	2.36	3.11
	H-BA	2.934	-0.651	-2.488	0.028	1.83	2.31	3.03
	H-BB	2.940	-0.658	1.716	0.026	1.66	2.15	2.87
WSiGeP_4	H-AA	3.452	-0.279	2.016	0.042	0.56	0.58	1.19
	H-AB	3.459	-0.259	-1.085	0.032	0.46	0.51	1.06
	H-BA	3.462	-0.271	-2.989	0.058	0.39	0.47	0.97
	H-BB	3.468	-0.262	2.031	0.043	0.25	0.42	0.75
WSiGeAs_4	H-AA	3.594	-0.113	2.103	0.096	0.41	0.45	0.89
	H-AB	3.599	-0.072	-1.204	0.084	0.33	0.39	0.82
	H-BA	3.601	-0.086	-3.104	0.124	0.28	0.36	0.76
	H-BB	3.605	-0.053	2.118	0.101	0.18	0.29	0.58

from Table I, all the considered phases are energetically feasible. Nevertheless, the ground state configurations are different. For instance, the H-BB phase is most favorable for WSiGeN_4 , but WSiGeP_4 and WSiGeAs_4 are most stable in the H-AA phase. The dynamical stability of these structures is verified by calculating phonon spectra (see section I of Supplemental Material (SM)). The absence of imaginary phonon mode in the entire BZ confirms the stability of phases H-AA, H-AB, H-BA, and H-BB. Furthermore, we have calculated the electric polarization using the Berry-phase method [53, 54]. There are two main factors contributing to the origin of vertical polarization. The first one is the asymmetry arising from the replacement of one Si by Ge atom, and another is the asymmetry arising from the rotation of Si-Z and Ge-Z layers (see Fig. 1(b)). Table I summarizes the calculated electric dipole moment per unit cell.

The three-dimensional band structures of the monolayer H-BB WSiGeN_4 and H-AA WSiGeP_4 are shown in Figs. 1(c) and 1(d), respectively (see section II of SM for WSiGeAs_4). The monolayer H-BB WSiGeN_4 has an indirect band gap with valence band maximum (VBM) and conduction band minimum (CBM) at Γ and K/K' points, respectively. The monolayer H-AA WSiGeP_4 , and WSiGeAs_4 are the direct band gap semiconductors with band edges located at K/K' points. The monolayer WSiGeN_4 , WSiGeP_4 and WSiGeAs_4 have valley-like peaks in the vicinity of K and K' points. The two valleys at K and K' are inequivalent due to structural asymmetry and time-reversal symmetry, although they have degenerate energy, as discussed in the coming sections.

B. Valley physics

To investigate the valleys in the monolayer WSiGeZ_4 , band structures with SOC are calculated as shown in

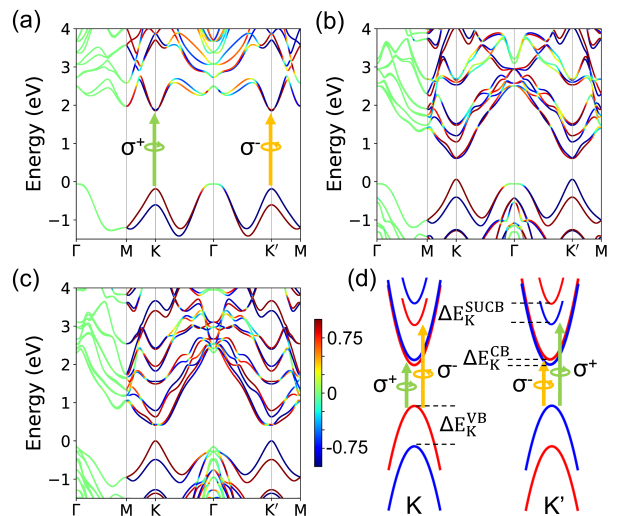


FIG. 2. The spin resolved band structure of monolayer (a) H-BB WSiGeN_4 , (b) H-AA WSiGeP_4 and (c) H-AA WSiGeAs_4 calculated using PBE functional with inclusion of SOC. (d) Schematic of valley selective excitation. Length of arrows and circles depict the energy and chirality of incident photon, respectively. The red and blue colors denotes the spin-up and spin-down states, respectively.

Figs. 2(a), 2(b) and 2(c). We have observed that monolayer H-BB WSiGeN_4 is still an indirect band semiconductor and monolayer H-AA WSiGeP_4 and WSiGeAs_4 remain direct band semiconductors. Band gaps obtained using PBE functional are listed in Table I. We have also used the more accurate HSE06 functional and G_0W_0 approach to validate the band structure results. The band structures are shown in section III and IV of SM, and the band gaps are compared in Table I. We have found that apart from the band gap, all the band features are similar irrespective of the choice of functional. The band gaps increase for the HSE06 and G_0W_0 methods due to the

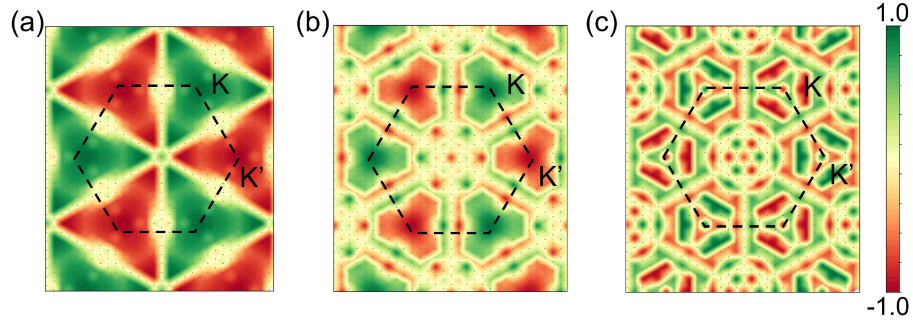


FIG. 3. The degree of circular polarization for transition between VB to CB in monolayer (a) H-BB WSiGeN₄ and (b) H-AA WSiGeP₄ mapped over the BZ. (c) The circular polarization for transition between VB to SUCB in monolayer H-AA WSiGeP₄. The black dotted lines represents the first BZ.

inclusion of exact exchange and self-energy, respectively. As seen in Figs. 2(a), 2(b) and 2(c), SOC mainly causes spin splitting of the degenerate bands. The spin splitting is a direct consequence of the inversion symmetry breaking, which lifts the spin degeneracy at each generic k -point. Since the time-reversal symmetry is preserved, the spin polarization at K and K' points are opposite because the time-reversal operation connects the K and K' points. Additionally, properties that are odd under time-reversal operation will have opposite natures at K and K' points. This concludes the existence of a valley degree of freedom.

The circular polarization for optical transition between the pair of states $|n\mathbf{k}\rangle$ and $|m\mathbf{k}\rangle$ is given by [55]

$$\eta(\mathbf{k}) = \frac{|M_+|^2 - |M_-|^2}{|M_+|^2 + |M_-|^2} \quad (2)$$

where M_{\pm} is the optical transition matrix element for the incident light with σ_{\pm} polarization. The M_{\pm} can be expressed as $M_{\pm} = \frac{1}{\sqrt{2}}(M_x \pm M_y)$, where $M_{x/y} = m_e \langle m\mathbf{k} | v_{x/y} | n\mathbf{k} \rangle$. $\eta = +1$ and $\eta = -1$ represent the optical absorption of only right hand circularly polarized (RHCP) and left hand circularly polarized (LHCP) light, respectively. Figure 3(a) shows the degree of circular polarization of excitation from first occupied valence band (VB) to first unoccupied conduction band (CB) in the case of monolayer H-BB WSiGeN₄. As seen, the circular dichroism is perfectly valley selective. The absorption of RHCP and LHCP photon will take place at K and K' points, respectively. Therefore, the circularly polarized optical pumping can control the electron and hole population of either valley. In the case of the monolayer H-BB WSiGeN₄, the direct band gap at K/K' point is 2.16 eV. Therefore, either valley can be selectively excited by the circularly polarized photon with the energy around 2.16 eV.

In case of monolayer H-AA WSiGeP₄ and WSiGeAs₄, the picture remains the same. However, there are no additional states apart from K/K' near the CBM and VBM, thus, there will be no scattering states. Figure 3(b) shows the circular polarization for optical transition between

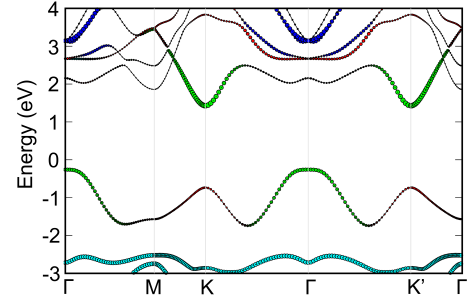


FIG. 4. Orbital projected band structure of monolayer H-BB WSiGeN₄ without SOC. Fermi level is set to zero in the energy axis. The fatness of band structure corresponds to $W-d_{z^2}$ (green), $W-d_{x^2-y^2}$ and $W-d_{xy}$ (red), $W-d_{yz}$ and $W-d_{xz}$ (blue), and N- p (cyan) orbitals.

VB to CB in the case of monolayer H-AA WSiGeP₄. The valleys are perfect and show complete valley contrasting physics, i.e., selective valley excitation. The valley selective optical transition occurs from VB to CB when the energy of the circularly polarized incident photon is around 0.56 and 0.41 eV for monolayer H-AA WSiGeP₄ and WSiGeAs₄, respectively. Furthermore, there exist additional valleys at the second unoccupied conduction band (SUCB) near the CBM (see Figs. 2(b) and 2(c)). Also, the spin polarization for the SUCB at K and K' points is opposite. Therefore, if the energy of the incident photon is greater than the direct band gap, then the transition from VBM to SUCM takes place (see Fig. 2(d)). The circular polarization from the VB to SUCM is also valley specified, as shown in Fig. 3(c). The LHCP and RHCP from VBM to SUCM will be absorbed at K and K' valleys, respectively. Note that the chirality of light for the transition taking place from VB to CB or VB to SUCB is opposite in the same valley (see Fig. 2(d)). Therefore, we can selectively pump an electron from VB to CB or SUCB by using optically selective light. This shows that SUCB in monolayer H-AA WSiGeP₄ and WSiGeAs₄ add another dimension to the valley physics.

The low power $\mathbf{k}\cdot\mathbf{p}$ Hamiltonian including the orbital

TABLE II. The observed spin splitting of VB (ΔE_K^{VB}), CB (ΔE_K^{CB}), SUCB (ΔE_K^{SUCB}) and the Berry curvature (Ω_K) at K point.

	Phase	ΔE_K^{VB} (meV)	ΔE_K^{CB} (meV)	ΔE_K^{SUCB} (meV)	Ω_K (\AA^2)
WSiGeN ₄	H-AA	415	3	-	16.1
	H-AB	415	4	-	17.2
	H-BA	417	9	-	17.5
	H-BB	418	12	-	18.1
WSiGeP ₄	H-AA	431	6	184	75
	H-AB	426	4	186	133
	H-BA	435	6	174	161
	H-BB	436	9	184	335
WSiGeAs ₄	H-AA	480	18	164	108
	H-AB	481	25	217	151
	H-BA	492	26	180	205
	H-BB	502	28	236	411

and spin degrees of freedom explains the valley splitting around C_3 symmetric K/K' points. Figure 4 shows the orbital-projected band structure of monolayer H-BB WSiGeN₄. The VB and SUCB states mainly consist of in-plane orbitals (d_{xy} , $d_{x^2-y^2}$). Whereas, the out-of-plane orbital (d_{z^2}) mainly contribute to the CBM. Similar contributions are also observed for monolayer H-AA WSiGeP₄ and WSiGeAs₄. The $\mathbf{k}\cdot\mathbf{p}$ model Hamiltonian employing the basis $|d_{xy}-\tau id_{x^2-y^2}\rangle \otimes |s_z\rangle$, $|d_{z^2}\rangle \otimes |s_z\rangle$ and $|d_{xy}+\tau id_{x^2-y^2}\rangle \otimes |s_z\rangle$ and containing the terms up to linear in \mathbf{k} is given by [27, 55, 56]

$$H_\tau = \begin{pmatrix} \epsilon_a + \tau\lambda_a S_z & \gamma_2 k^- & \gamma_1 k^+ \\ \gamma_2 k^+ & \epsilon_c & \gamma_3 k^- \\ \gamma_1 k^+ & \gamma_3 k^+ & \epsilon_v + \tau\lambda_v S_z \end{pmatrix} \quad (3)$$

where $k^\pm = k_x \pm \tau i k_y$ and k_x or k_y is measured from K and K' point. The $\tau = \pm 1$ is the valley index and γ_i are the optical matrix elements. The ϵ_c , ϵ_v , and ϵ_a are the energy levels at K/K' point. $\Delta = \epsilon_c - \epsilon_v$ is the direct band gap. $2\lambda_a$ (ΔE_K^{SUCB}) and $2\lambda_v$ (ΔE_K^{VB}) represent the spin splitting at the bottom of SUCB and the top of VB (see Fig. 2(d)). For the case of monolayer H-BB WSiGeN₄, SUCB is far away from the CBM. Therefore, the two band $\mathbf{k}\cdot\mathbf{p}$ Hamiltonian is sufficient, which reads as [27]

$$H_\tau = \begin{pmatrix} \epsilon_c & \gamma_3 k^- \\ \gamma_3 k^+ & \epsilon_v + \tau\lambda_v S_z \end{pmatrix} \quad (4)$$

To quantize the SOC effect, we have calculated the strength of the spin splitting at the top of the VB, the bottom of CB and SUCB (see Table II). The valley splitting observed for the top VB and SUCB is significantly larger than the lowest CB. The W- d_{xy} and W- $d_{x^2-y^2}$ orbitals under the influence of in-plane electric dipole moment produce spin splitting at the K point [57]. The CB is mainly contributed by W- d_{z^2} and the contributions from W- d_{xy} and W- $d_{x^2-y^2}$ are nearly zero. Therefore, spin splitting is predominant for the VB and the

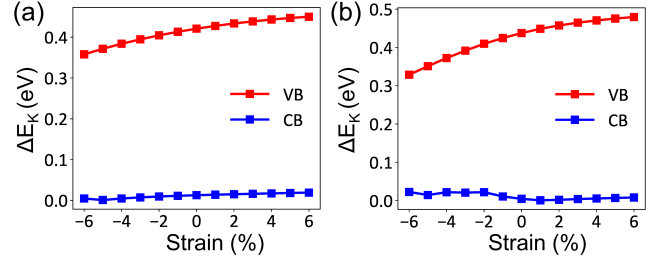


FIG. 5. The variation of spin splitting of the VB and CB at K/K' valleys with respect to the biaxial strain in monolayer (a) H-BB WSiGeN₄ and (b) H-AA WSiGeP₄.

SUCB, and very tiny for the CB. The trend for spin splitting at valleys is observed as WSiGeN₄ < WSiGeP₄ < WSiGeAs₄, which is attributed to the increase in SOC for heavier elements.

Incommensurate lattices can bring about interfacial strain during support on a substrate or vdW heterostructures formation. Therefore, the role of strain is also addressed in this study. We have applied the biaxial compressive and tensile strain in the deformation range of 6% to investigate the evolution of band edges. Figures 5(a), 5(b) and 5(c) show the variation of spin splitting at valleys of CB and VB for monolayer WSiGeZ₄. We see that the ΔE_K^{CB} is independent of the strain, whereas the ΔE_K^{VB} slightly increases (decreases) with the application of tensile (compressive strain).

C. Berry curvature modulation

To confirm the nonequivalence of valleys at K and K' points, we have studied the non-zero out-of-plane Berry curvatures. The velocity of the charge carriers in the presence of non-zero Berry curvature is given by $\hbar v_n(\mathbf{k}) = v_g - v_\perp$. Here, v_g denotes the group velocity, which is defined as $v_g = \nabla_{\mathbf{k}} \epsilon_n(\mathbf{k})$, where $\epsilon_n(\mathbf{k})$ is the energy of $|n\mathbf{k}\rangle$ state. In addition to the group velocity, Berry curvature leads to a transverse velocity denoted by v_\perp . The transverse velocity is given by $v_\perp = -\frac{e}{\hbar} \mathbf{E} \times \Omega_n(\mathbf{k})$, where \mathbf{E} is the in-plane electric field and $\Omega(\mathbf{k})$ is the out-of-plane Berry curvature [55]. For 2D systems, Berry curvature only has a z -component and for $|n\mathbf{k}\rangle$ state, it is expressed as [55]

$$\Omega_n(\mathbf{k}) = -2\text{Im} \sum_{n' \neq n} \frac{\langle n\mathbf{k}|v_x|n'\mathbf{k}\rangle \langle n'\mathbf{k}|v_y|n\mathbf{k}\rangle}{(\epsilon_{n'} - \epsilon_n)^2} \quad (5)$$

where the summation is over all the occupied bands. ϵ_n and $\epsilon_{n'}$ are the energy levels for $|n\mathbf{k}\rangle$ and $|n'\mathbf{k}\rangle$ states, respectively. The time-reversal operation applies the opposite Berry curvature at time-reversal conjugate momenta ($\Omega_n(-K) = -\Omega_n(K)$). Figures 6(a) and 6(b) show the Berry curvature of the VB and CB mapped in the first BZ for monolayer H-BB WSiGeN₄. Figures 6(c), 6(d) and 6(e) show the Berry curvature of monolayer H-AA

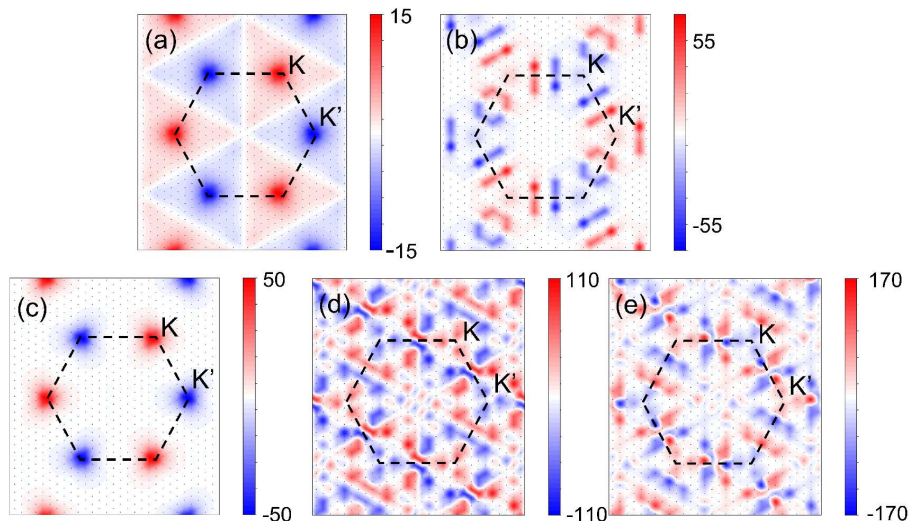


FIG. 6. Berry curvature distribution over BZ for (a) VB, (b) CB in monolayer H-BB WSiGeN₄. Berry curvature distribution of (c) VB, (d) CB and (e) SUCB in monolayer H-AA WSiGeP₄. The black dotted lines denote the first BZ.

WSiGeP₄ for VB, CB, and SUCB, respectively. Berry curvature is mostly confined around the valleys and has been found to be the highest at K and K' points. It has also been observed that the Berry curvature rapidly decreases to zero while moving away from the K and K' points. The opposite nature of Berry curvature near the K and K' points can distinguish the charge carriers at different valleys. The opposite Berry curvature leads to the spatial separation of charge carriers coupled with different valleys. Thus, the charge from different valleys will accumulate on opposite edges, leading to valley Hall effect. The time-reversal symmetry leads to the case of no net charge current at the linear order. However, there could exist a valley Hall effect after the electron doping. As for hole doping, one has to reach the energy level of K/K' point which is lower in energy compared to the Γ point for monolayer WSiGeN₄. The monolayer WSiGeP₄ and WSiGeAs₄ are more suitable for the case of hole doping, as the valence states lie at the K/K' point.

The transverse velocity can be amplified using the larger Berry curvature. Thus, faster charge transport and lesser recombination can be achieved. Therefore, a larger value of Ω_K is always desired, and Berry curvature modulation is indispensable in the field of valleytronics [58]. Using Eqs. 4 and 5, the Berry curvature of valence bands can be expressed as

$$\Omega_v(\mathbf{k}) = \tau \frac{2a^2 t^2 \Delta}{(4a^2 t^2 \mathbf{k}^2 + \Delta^2)^{3/2}} \quad (6)$$

where a , t and Δ are the lattice constant, nearest-neighbor hopping integral, and direct band gap, respectively. Therefore, the Berry curvature can be enhanced by tuning the parameters a , t and Δ . Figure 7(a), 7(b) and Table II show the modulation of Berry curvature via different stacking orders. Surprisingly, the Berry curvature can be enhanced up to 400% compared to its ground

state. For the case of monolayer H-AA WSiGeP₄, it increases Berry curvature from 80 \AA^2 to 335 \AA^2 by changing the phase to the H-BB. Similarly, Berry curvature is also enhanced to 411 \AA^2 for monolayer H-BB WSiGeAs₄. However, modification is almost negligible in the case of monolayer H-BB WSiGeN₄ due to the small size of the N atom. The H-BB phase has the smallest value of Δ at the K point, thereby highest Berry curvature is obtained for this phase. The percentage change in the direct gap is highest in the case of the WSiGeAs₄ monolayer, therefore, the strongest tuning is obtained using symmetry control for WSiGeAs₄ monolayer.

It is crucial to understand the underlying mechanism behind the Berry curvature modulation. The two main factors affecting SOC are macroscopic charge transfer and microscopic orbital contribution [59]. Table III shows the orbital contribution at K point for the VB for monolayer WSiGeP₄. A similar trend is also observed for the monolayer WSiGeAs₄ and WSiGeN₄. The W- d and P- p orbitals contribute to valence states, where W- d_{xy} and W- $d_{x^2-y^2}$ have the largest contributions. Rotation of Si/Ge-Z layers leads to a change in the orbital contribution, hence, the strength of the SOC. The contribution coming from heavy W- d is highest in the case of the H-BB phase. Thus, the highest SOC strength leads to the largest strength of Berry curvature at the K/K' point for the H-BB phase. The contribution of W- d orbitals follows the trend, H-BB > H-BA > H-AB > H-AA and the same trend is followed by the Berry curvature. This shows that microscopic orbital contribution has a strong correlation with the Berry curvature.

Another efficient way to modify the orbital contribution is by applying strain [58, 60]. Hence, the effect of tensile and compressive biaxial strain on the Berry curvature of VB is also analyzed. Figures 7(c) and 7(d) show the Berry curvature of unstrained and strained

TABLE III. Orbital contribution to the valence band at K/K' point of monolayer H-AA WSiGeP₄.

Phase	p_x	p_y	p_z	d_{xy}	d_{yz}	d_{z^2}	d_{xz}	$d_{x^2-y^2}$
H-AA	0.055	0.000	0.055	0.271	0.002	0.000	0.002	0.271
H-AB	0.055	0.009	0.055	0.271	0.003	0.002	0.003	0.271
H-BA	0.058	0.013	0.058	0.280	0.004	0.001	0.004	0.280
H-BB	0.057	0.025	0.057	0.303	0.001	0.000	0.001	0.303

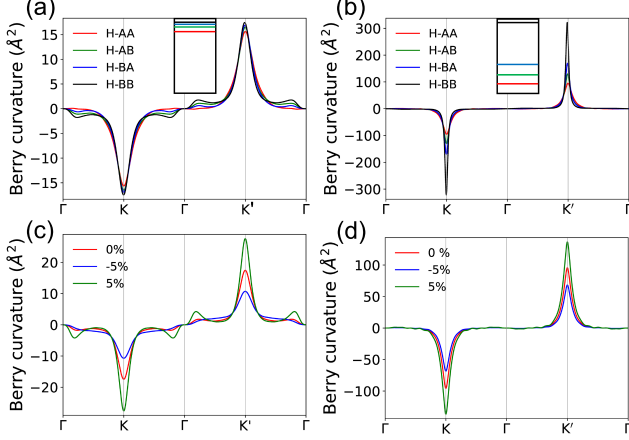


FIG. 7. Modulation of Berry curvature by varying stacking orders in monolayer (a) WSiGeN₄ and (b) WSiGeP₄ along the high symmetry line Γ -K- Γ -K'- Γ . The insets in (a) and (b) show the position of Berry curvature at K' point. The effect of biaxial strain on the Berry curvature in monolayer (c) H-BB WSiGeN₄ and (d) H-AA WSiGeP₄.

cases for the VB in monolayer H-BB WSiGeN₄ and H-AA WSiGeP₄. The strain could also tune the Berry curvature efficiently. Under the tensile strain, the direct band gap and the magnitude of wavevector are reduced. Therefore, the magnitude of the Berry curvature increases. In the case of WSiGeN₄, Berry curvature increases from 15 Å² to 25 Å² under 5% tensile strain. Whereas, it increases from 80 Å² to 129 Å² in WSiGeP₄ and is significantly smaller than the Berry curvature 335 Å² obtained by symmetry control.

D. Rashba effect

The presence of strong SOC in addition to the breaking of surface inversion symmetry along z -direction leads to the Rashba spin splitting of VB around Γ point. The spin-projected band structure of top VBs of monolayer H-AA WSiGeP₄ is depicted in Fig. 8(a). The bands describe unique Rashba type dispersion, which can be explained by linear Rashba Hamiltonian. The helical nature of in-plane spin textures as shown in Fig. 8(b), confirms the presence of the Rashba effect around the Γ point. Moreover, a small out-of-plane spin component has three-fold rotation symmetry in-line with the sym-

metry of the crystal.

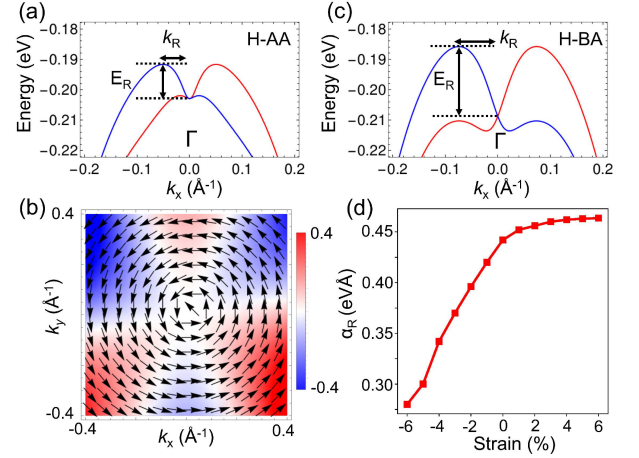


FIG. 8. (a) The spin-projected band structures and (b) associated spin texture of top valence bands in H-AA WSiGeP₄. The arrows and color represent the in-plane (x, y) and out-of-plane (z) components of spin textures, respectively. (c) The spin-projected band structure of top valence bands in H-BA WSiGeP₄. (d) The variation of Rashba coefficients under the application of biaxial strain.

To understand the band structure and spin texture, we have constructed a $\mathbf{k}\cdot\mathbf{p}$ model Hamiltonian near the Γ point. The little group of the Γ point is C_{3v} , and the corresponding Hamiltonian is expressed as [61–63]

$$H_{\Gamma}(\mathbf{k}) = H_o(\mathbf{k}) + \alpha_R(k_x\sigma_y - k_y\sigma_x) + \gamma(k_y^3 - 3k_xk_y^2) \quad (7)$$

where $H_o(k)$ is the free particle Hamiltonian, and α_R is the linear Rashba coefficient. γ is the parameter signifying the contributions from the cubic term in the splitting and takes the out-of-plane spin contributions into consideration. We have observed that the energy contribution coming from the cubic term is much smaller than the linear term. The fitting of the DFT band structure by $\mathbf{k}\cdot\mathbf{p}$ model hamiltonian allows the calculation of α_R . Within the linear Rashba term, the α_R is also estimated by $\alpha_R = \frac{2E_R}{k_R}$, where E_R and k_R are the Rashba energy splitting and momentum shift, respectively [61]. E_R and k_R are schematically shown in Fig. 8(a). The calculated values of E_R and k_R are 11.2 meV and 0.55 Å⁻¹, respectively. Thus, for monolayer H-AA WSiGeP₄, α_R is 0.41 eVÅ. A larger value of α_R makes the Rashba effect more accessible experimentally. Therefore, greater magnitude

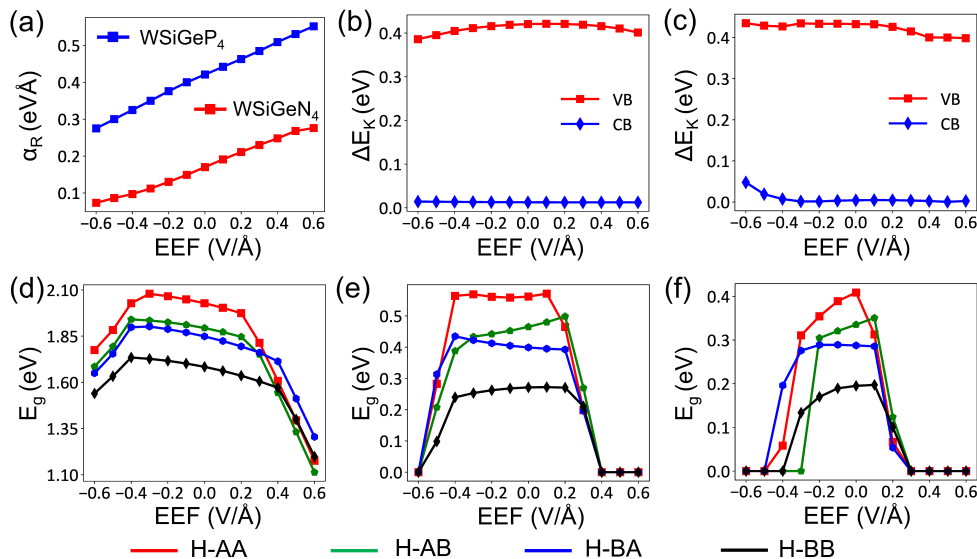


FIG. 9. (a) The variation of Rashba coefficient (α_R) under the application of out-of-plane EEF. Zeeman spin splittings at K/K' points as a function of EEF in monolayer (b) H-BB WSiGeN₄ and (c) H-AA WSiGeP₄. Modulation of band gaps with strain in monolayer (d) H-BB WSiGeN₄, (e) H-AA WSiGeP₄ and (f) H-AA WSiGeAs₄.

of α_R is always desired. Consequently, we have studied the impact of symmetry on the strength of Rashba effect. Table IV shows E_R , k_R , and α_R of monolayer WSiGeN₄ and WSiGeP₄ in different configurations. H-BA structure has the largest value of E_R and α_R . As shown in Fig. 8(c), E_R increases to 22.9 meV from 11.2 meV when the structure changes to H-BA from H-AA. The value of α_R is also significantly enhanced from 0.41 eVÅ to 0.61 eVÅ. Similar results have also been obtained for WSiGeN₄ and WSiGeAs₄. The observed trend of α_R is H-BA > H-BB > H-AA > H-AB.

According to the Rashba model, spin splitting occurs in the plane perpendicular to the electric field. The net vertical electric field acting on the metal atom W, determines the strength of the Rashba effect. Therefore, the larger the out-of-plane intrinsic electric field, the more prominent is the in-plane spin splitting. In case of H-BA, the out-of-plane intrinsic electric field arising due to the formation of Janus and the position of Z atoms support each other. Therefore, the strongest Rashba spin splitting is observed for the H-BA phase as it has the highest out-of-plane asymmetry.

Additionally, the effect of biaxial strain on α_R is also studied, and the variation is shown in Fig. 8(d). The value of α_R decreases from 0.41 eVÅ to 0.28 eVÅ under a compressive strain of 6%. The tensile strain of 6% increase α_R to 0.46 eVÅ, which is significantly smaller than the increment observed using the symmetry control. The strain is also an effective way to modulate the band edge positions and band gaps. The complete band structures under the application of biaxial strain are shown in section VI of SM. For the case of WSiGeN₄, the band gap remains indirect in the range of -6% to 6%. The band gap remains direct for WSiGeP₄ and WSiGeAs₄ in the range

TABLE IV. The calculated parameters (E_R , k_R and α_R) for Rashba spin splitting around Γ point.

	Phase	E_R (meV)	k_R (Å ⁻¹)	α_R (eVÅ)
WSiGeN ₄	H-AA	5.7	0.060	0.19
	H-AB	3.0	0.068	0.09
	H-BA	9.4	0.067	0.28
	H-BB	5.6	0.066	0.17
WSiGeP ₄	H-AA	11.2	0.055	0.41
	H-AB	8.57	0.079	0.22
	H-BA	22.9	0.075	0.61
	H-BB	16.9	0.079	0.43

of -3% to 3%. In general, the band gap shows decrement under tensile strain. However, under compressive strain, the band gap increases up to 2% and decreases afterward. Furthermore, WSiGeAs₄ shows semiconductor to metal transitions under a compressive strain of larger than 3%.

E. The role of electric field

An external electric field (EEF) is commonly used to modify the strength of Rashba effect in spintronics devices [64, 65]. Therefore, the effect of EEF is also investigated in this study. We have applied the out-of-plane EEF in the range of -0.6 V/Å to 0.6 V/Å to analyze the variation of Rashba coefficient (α_R) and Zeeman splittings (ΔE_K^{CB} and ΔE_K^{VB}). Figure 9(a) shows the variation of α_R as a function of EEF for monolayer H-BB WSiGeN₄ and H-AA WSiGeP₄. When the EEF points from Ge to Si (taken to be positive direction), which is consistent with the local electric field, it enhances the

TABLE V. The acoustic phonon limited carrier mobility and other relevant parameters for WSiGeZ₄ monolayer. The x and y directions correspond to armchair and zigzag directions, respectively. m_o is rest mass of the electron.

	Carrier	m_x/m_o	m_y/m_o	E_x (eV)	E_y (eV)	C_{2D} (Nm ⁻¹)	μ_x (cm ² V ⁻¹ s ⁻¹)	μ_y (cm ² V ⁻¹ s ⁻¹)
WSiGeN ₄	e_K	0.460	0.499	5.82	6.832	493.1	2355.1	942.2
	h_Γ	1.838	1.816	5.70	5.147	493.1	98.3	119.7
WSiGeP ₄	e_K	0.975	0.594	13.18	10.32	225.5	37.3	99.9
	h_K	0.484	0.448	9.49	6.98	225.5	237.0	473.5
WSiGeAs ₄	e_K	3.260	1.673	11.92	10.88	178.2	3.5	8.2
	h_K	0.542	0.477	9.59	8.91	178.2	150.1	197.6

Rashba SOC. Whereas, the opposite direction of EEF reduces the strength of Rashba SOC, as the effects of the EEF and the local electric field cancel each other. The value of α_R varies from 0.28 eVÅ to 0.55 eV/Å in case of monolayer H-AA WSiGeP₄, while it varies from 0.08 eV/Å to 0.25 eV/Å for monolayer H-BB WSiGeN₄. The variation of Zeeman splittings at the K point are shown in Figs. 9(b) and 9(c). The $d_{x^2-y^2}$ and d_{xy} orbitals under the influence of in-plane electric field contribute to the Zeeman splitting at K point. Therefore, the out-of-plane EEF hardly affects the ΔE_K^{CB} and ΔE_K^{VB} . The evolution of band gap as a function of EEF is provided in Figs. 9(d), 9(e) and 9(f) (see section V of SM for band structures). We have noticed that the band gaps are almost insensitive to small EEFs (in the range -0.3 V/Å to 0.3 V/Å). It is also interesting to note that the CBM for monolayer WSiGeZ₄ shifts to the M point under large EEF (see section VI of SM), this is because the Si atom starts contributing to the CBM. Therefore, band gaps decrease sharply under large EEFs. In the case of WSiGeP₄ and WSiGeAs₄, giant Stark effect closes the band gap and semiconductor to metal transition takes place.

F. Carrier mobility

Estimation of carrier mobilities is essential for exploring the potential use of any material for application in electronic devices [23, 66]. The carrier mobility (μ_{2D}) of the WSiGeZ₄ monolayer is calculated using the deformation potential (DP) theory. According to DP theory [67], μ_{2D} is expressed as

$$\mu_{2D} = \frac{e\hbar^3 C_{2D}}{k_B T m^* m_d E_l^2} \quad (8)$$

where m_d and m^* are the average effective mass ($\sqrt{m_x m_y}$) and the effective mass along the transport direction, respectively. C_{2D} is Young's elastic modulus, which is calculated from the elastic tensor C_{ij} . The E_l is the DP constant defined by $E_l = \delta E / \delta l$. Here, δE is the change in the position of the CBM or VBM with respect to the vacuum level and $\delta l = \Delta l / l$ is the relative strain. The detailed analysis of the method used to compute elastic constants and carrier mobilities is discussed

in section VI of SM. The calculated elastic constants and carrier mobilities are listed in Table V. The carrier mobilities in these monolayers are anisotropic and show considerable variation. For instance, the most significant carrier mobility observed is 2355.1 cm²V⁻¹s⁻¹ for the electron in monolayer H-BB WSiGeN₄, and the smallest carrier mobility observed is as tiny as 3.514 cm²V⁻¹s⁻¹ for the electron in monolayer H-AA WSiGeAs₄.

IV. CONCLUSION

We have revealed that different stacking patterns of Si-Z, Z-W-Z and Ge-Z generate the dynamically stable structures. The most stable structure for monolayer WSiGeN₄ is H-BB, whereas for monolayer WSiGeP₄ and WSiGeAs₄ is H-AA. These materials show valley contrasting circular dichroism, spin-valley coupling, and Berry curvature. Additionally, the out-of-plane asymmetry in them leads to Rashba effect around the center of the BZ. The stacking pattern greatly modifies the spintronics and valleytronics properties. The highest Rashba spin-orbit coupling around the Γ point is observed for the H-BA phase having the highest out-of-plane electric dipole moment. Whereas, the Berry curvature is strongest at valleys for H-BB phase with the highest contribution coming from d_{xy} and $d_{x^2-y^2}$ orbitals. Additionally, valleys observed in WSiGeP₄ and WSiGeAs₄ monolayers at K and K' points have multiple folds. Furthermore, we have found that the band gap type and valleys can be tuned with an EEF and biaxial strain. Under large strain and high electric field, monolayer WSiGeP₄ and WSiGeAs₄ show semiconductor to metal transition. We have found the strong anisotropy in carrier mobilities along the armchair and zigzag directions. Rashba spin splitting and valley polarization can facilitate the manipulation of electron spin and valley. The regulation of spin direction of separated valley carriers by controlling symmetry can be realized better in septuple-atomic-layer materials compared to TMDs.

ACKNOWLEDGEMENTS

S.S. acknowledges CSIR, India, for the senior research fellowship [grant no. 09/086(1432)/2019-EMR-I]. A.P. acknowledges IIT Delhi for the senior research fellowship. R.M. acknowledges CSIR, India, for the junior research

fellowship [grant no. 09/0086(12865)/2021-EMR-I]. S. B. acknowledges financial support from SERB under a core research grant (grant no. CRG/2019/000647) to set up his High Performance Computing (HPC) facility “Veena” at IIT Delhi for computational resources.

-
- [1] A. K. Geim, *Science* **324**, 1530 (2009).
- [2] K. S. Novoselov, L. Colombo, P. Gellert, M. Schwab, and K. Kim, *Nature* **490**, 192 (2012).
- [3] C. L. Kane and E. J. Mele, *Phys. Rev. Lett.* **95**, 226801 (2005).
- [4] A. Molle, C. Grazianetti, L. Tao, D. Taneja, M. H. Alam, and D. Akinwande, *Chem. Soc. Rev.* **47**, 6370 (2018).
- [5] Z. Ni, Q. Liu, K. Tang, J. Zheng, J. Zhou, R. Qin, Z. Gao, D. Yu, and J. Lu, *Nano Lett.* **12**, 113 (2012).
- [6] N. G. Chopra, R. Luyken, K. Cherrey, V. H. Crespi, M. L. Cohen, S. G. Louie, and A. Zettl, *Science* **269**, 966 (1995).
- [7] S. Manzeli, D. Ovchinnikov, D. Pasquier, O. V. Yazyev, and A. Kis, *Nat. Rev. Mater.* **2**, 1 (2017).
- [8] X. Xu, W. Yao, D. Xiao, and T. F. Heinz, *Nat. Phys.* **10**, 343 (2014).
- [9] G. Wang, A. Chernikov, M. M. Glazov, T. F. Heinz, X. Marie, T. Amand, and B. Urbaszek, *Rev. Mod. Phys.* **90**, 021001 (2018).
- [10] F. Liang, C. Zhang, and Z. Yang, *Adv. Mater.* **26**, 6944 (2014).
- [11] R. Li, Y. Cheng, and W. Huang, *Small* **14**, 1802091 (2018).
- [12] T. Hu, F. Jia, G. Zhao, J. Wu, A. Stroppa, and W. Ren, *Phys. Rev. B* **97**, 235404 (2018).
- [13] S. B. Touski and N. Ghobadi, *Phys. Rev. B* **103**, 165404 (2021).
- [14] A. Singh, M. Jain, and S. Bhattacharya, *Nanoscale Adv.* **3**, 2837 (2021).
- [15] J. Yuan, Y. Yang, Y. Cai, Y. Wu, Y. Chen, X. Yan, L. Shen, *et al.*, *Physical Review B* **101**, 094420 (2020).
- [16] L. Dong, J. Lou, and V. B. Shenoy, *ACS nano* **11**, 8242 (2017).
- [17] A.-Y. Lu, H. Zhu, J. Xiao, C.-P. Chuu, Y. Han, M.-H. Chiu, C.-C. Cheng, C.-W. Yang, K.-H. Wei, Y. Yang, *et al.*, *Nature nanotechnology* **12**, 744 (2017).
- [18] C. W. Jang, W. J. Lee, J. K. Kim, S. M. Park, S. Kim, and S.-H. Choi, *NPG Asia Materials* **14**, 1 (2022).
- [19] L. Wang, Y. Shi, M. Liu, A. Zhang, Y.-L. Hong, R. Li, Q. Gao, M. Chen, W. Ren, and H.-M. Cheng, *Nat. Commun.* **12**, 1 (2021).
- [20] Y.-L. Hong, Z. Liu, L. Wang, T. Zhou, W. Ma, C. Xu, S. Feng, L. Chen, M.-L. Chen, and D.-M. Sun, *Science* **369**, 670 (2020).
- [21] S.-D. Guo, Y.-T. Zhu, W.-Q. Mu, and X.-Q. Chen, *Journal of Materials Chemistry C* **9**, 7465 (2021).
- [22] A. Rezavand, N. Ghobadi, and B. Behnamghader, *Physical Review B* **106**, 035417 (2022).
- [23] S.-D. Guo, W.-Q. Mu, Y.-T. Zhu, R.-Y. Han, and W.-C. Ren, *Journal of Materials Chemistry C* **9**, 2464 (2021).
- [24] G. Hussain, A. Samad, M. U. Rehman, G. Cuono, and C. Autieri, *Journal of Magnetism and Magnetic Materials*, 169897 (2022).
- [25] D. Dey, A. Ray, and L. Yu, *Physical Review Materials* **6**, L061002 (2022).
- [26] S.-D. Guo, W.-Q. Mu, J.-H. Wang, Y.-X. Yang, B. Wang, and Y.-S. Ang, *Physical Review B* **106**, 064416 (2022).
- [27] D. Xiao, G.-B. Liu, W. Feng, X. Xu, and W. Yao, *Phys. Rev. Lett.* **108**, 196802 (2012).
- [28] R. Islam, B. Ghosh, C. Autieri, S. Chowdhury, A. Bansil, A. Agarwal, and B. Singh, *Phys. Rev. B* **104**, L201112 (2021).
- [29] R. Battilomo, N. Scopigno, and C. Ortix, *Phys. Rev. Lett.* **123**, 196403 (2019).
- [30] S. Hurand, A. Jouan, C. Feuillet-Palma, G. Singh, J. Biscaras, E. Lesne, N. Reyren, A. Barthélémy, M. Bibes, J. Villegas, *et al.*, *Scientific reports* **5**, 1 (2015).
- [31] S. Sheoran, M. Kumar, P. Bhumla, and S. Bhattacharya, *Mater. Adv.* **3**, 4170 (2022).
- [32] S. Sheoran, P. Bhumla, and S. Bhattacharya, *Phys. Rev. Materials* **6**, 094602 (2022).
- [33] D. Xiao, W. Yao, and Q. Niu, *Physical review letters* **99**, 236809 (2007).
- [34] R. Ahammed and A. De Sarkar, *Physical Review B* **105**, 045426 (2022).
- [35] K.-H. Jin, E. Oh, R. Stania, F. Liu, and H. W. Yeom, *Nano Lett.* **21**, 9468 (2021).
- [36] G. Kresse and J. Furthmüller, *Phys. Rev. B* **54**, 11169 (1996).
- [37] P. E. Blöchl, *Phys. Rev. B* **50**, 17953 (1994).
- [38] G. Kresse and D. Joubert, *Phys. Rev. B* **59**, 1758 (1999).
- [39] J. P. Perdew, K. Burke, and M. Ernzerhof, *Phys. Rev. Lett.* **77**, 3865 (1996).
- [40] A. Togo and I. Tanaka, *Scr. Mater.* **108**, 1 (2015).
- [41] A. A. Mostofi, J. R. Yates, G. Pizzi, Y.-S. Lee, I. Souza, D. Vanderbilt, and N. Marzari, *Computer Physics Communications* **185**, 2309 (2014).
- [42] J. Heyd, G. E. Scuseria, and M. Ernzerhof, *The Journal of chemical physics* **118**, 8207 (2003).
- [43] L. Hedin, *Phys. Rev.* **139**, A796 (1965).
- [44] M. S. Hybertsen and S. G. Louie, *Phys. Rev. Lett.* **55**, 1418 (1985).
- [45] S. Albrecht, L. Reining, R. Del Sole, and G. Onida, *Phys. Rev. Lett.* **80**, 4510 (1998).
- [46] S. Sheoran, D. Gill, A. Phutela, and S. Bhattacharya, *arXiv:2208.00127* (2022).
- [47] S. Sheoran, S. Monga, A. Phutela, and S. Bhattacharya, *J. Phys. Chem. Lett.* **14**, 1494 (2023).
- [48] W. Zhou, L. Wu, A. Li, B. Zhang, and F. Ouyang, *The Journal of Physical Chemistry Letters* **12**, 11622 (2021).
- [49] L. Kang and Z. Lin, *Physical Review B* **103**, 195404 (2021).
- [50] L. Wang, Y. Jiang, J. Liu, S. Zhang, J. Li, P. Liu, Y. Sun, H. Weng, and X.-Q. Chen, *Physical Review B* **106**, 155144 (2022).

- [51] Y.-T. Ren, L. Hu, Y.-T. Chen, Y.-J. Hu, J.-L. Wang, P.-L. Gong, H. Zhang, L. Huang, and X.-Q. Shi, *Physical Review Materials* **6**, 064006 (2022).
- [52] S.-D. Guo, Y.-T. Zhu, W.-Q. Mu, L. Wang, and X.-Q. Chen, *Computational Materials Science* **188**, 110223 (2021).
- [53] R. King-Smith and D. Vanderbilt, *Physical Review B* **47**, 1651 (1993).
- [54] N. A. Spaldin, *Journal of Solid State Chemistry* **195**, 2 (2012).
- [55] C. Yang, Z. Song, X. Sun, and J. Lu, *Phys. Rev. B* **103**, 035308 (2021).
- [56] S. Li, W. Wu, X. Feng, S. Guan, W. Feng, Y. Yao, and S. A. Yang, *Phys. Rev. B* **102**, 235435 (2020).
- [57] H. Lee and H. J. Choi, *Phys. Rev. B* **86**, 045437 (2012).
- [58] D. Tian, Z. Liu, S. Shen, Z. Li, Y. Zhou, H. Liu, H. Chen, and P. Yu, *Proceedings of the National Academy of Sciences* **118**, e2101946118 (2021).
- [59] W. Zhou, J. Chen, B. Zhang, H. Duan, and F. Ouyang, *Physical Review B* **103**, 195114 (2021).
- [60] J. Son, K.-H. Kim, Y. Ahn, H.-W. Lee, and J. Lee, *Physical review letters* **123**, 036806 (2019).
- [61] S.-B. Yu, M. Zhou, D. Zhang, and K. Chang, *Physical Review B* **104**, 075435 (2021).
- [62] F. Li, W. Wei, H. Wang, B. Huang, Y. Dai, and T. Jacob, *The journal of physical chemistry letters* **10**, 559 (2019).
- [63] P. Bhumla, D. Gill, S. Sheoran, and S. Bhattacharya, *J. Phys. Chem. Lett.* **12**, 9539 (2021).
- [64] C. Cheng, J.-T. Sun, X.-R. Chen, H.-X. Fu, and S. Meng, *Nanoscale* **8**, 17854 (2016).
- [65] Q.-F. Yao, J. Cai, W.-Y. Tong, S.-J. Gong, J.-Q. Wang, X. Wan, C.-G. Duan, and J. Chu, *Physical review B* **95**, 165401 (2017).
- [66] A. Priyadarshi, Y. S. Chauhan, S. Bhowmick, and A. Agarwal, *Nanoscale* (2022).
- [67] S. Bruzzone and G. Fiori, *Applied Physics Letters* **99**, 222108 (2011).